Dynamical diffraction of high-energy electrons investigated by focal series momentum-resolved scanning transmission electron microscopy at atomic resolution

Dynamical diffraction of high-energy electrons investigated by focal series momentum-resolved scanning transmission electron microscopy at atomic resolution

H. L. Robert[a,b,*], I. Lobato[c], F. J. Lyu[d], Q. Chen[d], S. Van Aert[c], D. Van Dyck[c], K. Müller-Caspary[a,e]

[a] *Ernst Ruska-Centre for Microscopy and Spectroscopy with Electrons (ER-C), Forschungszentrum Jülich, 52425 Jülich, Germany*
[b] *2nd Institute of Physics, RWTH Aachen University, 52074 Aachen, Germany*
[c] *Electron Microscopy for Materials Science (EMAT), University of Antwerp, Groenenborgerlaan 171, 2020 Antwerp, Belgium*
[d] *Key Laboratory for the Physics and Chemistry of Nanodevices, Department of Electronics, Peking University, Beijing 100871, China*
[e] *Department of Chemistry, Ludwig-Maximilians-Universität München, Butenandtstrasse 5-13, 81377 Munich, Germany*

Abstract

We report a study of scattering dynamics in crystals employing momentum-resolved scanning transmission electron microscopy under varying illumination conditions. As we perform successive changes of the probe focus, multiple real-space signals are obtained in dependence of the shape of the incident electron wave. With support from extensive simulations, each signal is shown to be characterized by an optimum focus for which the contrast is maximum and which differs among different signals. For instance, a systematic focus mismatch is found between images formed by high-angle scattering, being sensitive to thickness and chemical composition, and the first moment in diffraction space, being sensitive to electric fields. It follows that a single recording at one specific probe focus is usually insufficient to characterise materials comprehensively. Most importantly, we demonstrate in experiment and simulation that the second moment $(\mu_{20} + \mu_{02}) = \langle p^2 \rangle$ of the diffracted intensity exhibits a contrast maximum when the electron probe is focused at the top and bottom faces of the specimen, making the presented concept attractive for measuring local topography. Given the versatility of $\langle p^2 \rangle$, we furthermore present a detailed study of its large-angle convergence both analytically using the Mott scattering approach, and by dynamical simulations using the multislice algorithm including thermal diffuse scattering. Both approaches are in very good agreement and yield logarithmic divergence with increasing scattering angle.

Keywords: Optical sectioning, Momentum-resolved STEM, 4D-STEM, Aberration-correction, Momentum transfer

Introduction

In recent years, the field of scanning transmission electron microscopy (STEM) has benefited drastically from instrumental advances, following a trend towards increasing the number of simultaneously exploited information channels. For example, new electron scattering methods have been introduced, allowing the retrieval of structure, composition and electrostatic potential in thin crystals down to atomic level and below, using aberration-correction. In that regard, ultrafast electron cameras [1–8] have enabled the recording of a 2D diffraction pattern for each position of a 2D scan raster in a routine experiment. Such four-dimensional approaches, yielding information both in real and momentum space, can serve for the fundamental study of momentum-dependent scattering [9], as well as for the development of new methodologies for the structural and compositional characterisation of nanostructures [10]. In addition, ptychographic reconstruction algorithms [11–15] have enabled phase retrieval to be done with super-resolution [16–18], leading to insights into the atomic-scale electrostatic potentials of thin specimens. Finally, the direct evaluation of atomic and polarisation-induced electric fields, involving the calculation of the first moment in diffraction space [19–21], has been a crucial step in interpreting electron picodiffraction.

This yet incomplete set of examples shows that the comprehensive characterisation of thin specimens, for which the interaction can be described by the phase approximation, now stands within the reach of contemporary momentum-resolved STEM (MR-STEM). The flexibility of generating dedicated signals exploiting pre-determined regions of diffraction space post-recording, therefore, implies this new imaging mode to be considered universal [22, 23]. Nevertheless, especially when going beyond the framework of such thin samples, the coupling of the incident wave function to states within the crystal becomes another governing factor in determining the scattering dynamics. The contrast obtained by evaluating specific scattering angles is then expected to display a strong dependence on the boundary conditions at the specimen surfaces. In that respect, a STEM instrument can serve as a versatile set-up to vary the illumination of the specimen systematically, in particular by changing the vertical

*Corresponding author. Email: h.robert@fz-juelich.de

depth at which the electron wave is focused. It thus allows to study the response of the multidimensional set of data to a change in the distance between this depth and the interfaces with vacuum, while presenting an opportunity to measure their vertical location.

Whereas focus variation has frequently been used to obtain three-dimensional information employing high- [24–28] and low-angle [29, 30] electron scattering, it is currently being explored within the framework of four-dimensional STEM data in more specific applications [31, 32]. In addition to established detector geometries where the diffracted intensity is integrated over discs or (segmented) annuli, the high sampling in momentum space allows the retrieval of more advanced, 4D STEM-specific, signals. An example can be found in the calculation of the nth moments in diffraction space, with the first-order case being related to the average momentum transferred to the electron wave by interacting with the specimen. A systematic study that sheds light on the response of individual momentum space signals to a change of the incident wave function is therefore highly desirable.

To this end, we establish focal series MR-STEM (FS-MR-STEM) as a versatile concept in both experiment and simulation. A case study, based on α-In_2Se_3 nanosheets, is used to illustrate the individual focus dependencies of the first and second moments in diffraction space, as well as of conventional STEM signals formed by annular and disc-shaped detectors. In the first part, experiments reveal different optimum foci for, e.g., the first moment, Z-contrast and the second moment ($\mu_{20} + \mu_{02}$). Besides important practical consequences concerning processing and recording of four- and five-dimensional data, we emphasise the correspondence of signal- and focus-dependent contrast features to structural parameters. For example, contrast maxima of the second moment are observed when focusing the incident probe closely to the top and the bottom surface of a specimen. This presents an opportunity to perform direct surface detection using a focal series in a momentum-resolved set-up.

In the second part, we use comprehensive simulations to understand and validate the experimental findings. Conclusions are drawn with respect to specimen thickness variations in a systematic manner. In particular, we investigate the high-angle convergence of the second moment both analytically by considering Mott scattering and in dynamical simulations. This paper closes with a comprehensive discussion and a summary.

1. Experimental and simulation details

1.1. Experimental details

Nanosheets of $\alpha-In_2Se_3$ were prepared by exfoliation from a bulk crystal [34] whose unit cell is drawn in Fig. 1, together with a high-angle annular dark field (HAADF) Z-contrast image recorded in [001] projection. The schematic in Fig. 2 depicts the experimental set-up, including the

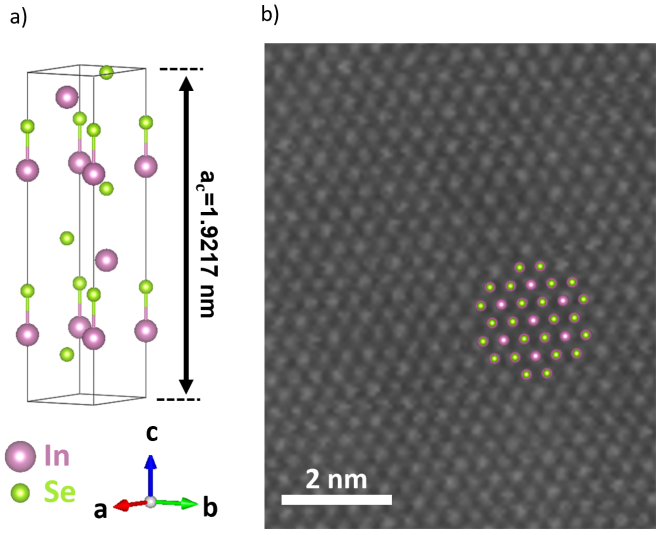

Figure 1: a) Crystallographic unit cell of α-In_2Se_3[33]. b) A HAADF image recorded in [001] zone axis, using a dedicated STEM detector, where the lateral positions of both atomic column types (either InSe or $InSe_2$) are depicted schematically.

probe rastering a 3D volume, the interaction with the specimen, the diffraction pattern recording and the schematic focus-dependent contrast of selected signals. Experiments have been performed using a probe-corrected FEI Titan 80-300 microscope, operated at an acceleration voltage of 200 kV, and equipped with a 256×256 pixels Medipix Merlin for EM camera [5]. A semi-convergence of $\alpha = 23$ mrad was measured for the incident probe, and the pixel size of the camera could be determined to be 0.21±0.01 mrad. The average of all recorded diffraction patterns can be found in Fig. 15 of appendix A.

The component object model (COM) interface of the microscope [35] was used to program the automated recording of FS-MR-STEM scans by python-based software control. A series of 21 different foci with a focus step of 1.5 nm was acquired, covering a total focus range of 30 nm. By convention, negative foci correspond to the probe being focussed to a point below the specimen entrance surface, positive ones to a point above. Distinct sets of real space images, corresponding to estalished dedicated STEM signals, were extracted from the raw diffraction data. Due to the Medipix frame rate of 2 kHz, which is still relatively low compared to typical scan speeds in a conventional STEM experiment, we used a scan raster of 64×64 positions with a pixel size of 31±1 pm. The total acquisition time was thus approximately 40 s.

The thickness of the specimen was measured to (7±1)a_c, with a_c=1.92 nm, and its mistilt from zone axis [001] to 1.7±0.5 mrad. Furthermore, specimen damage happening through the acquisition was found to be negligible. The details of these measurements are available in appendix A.

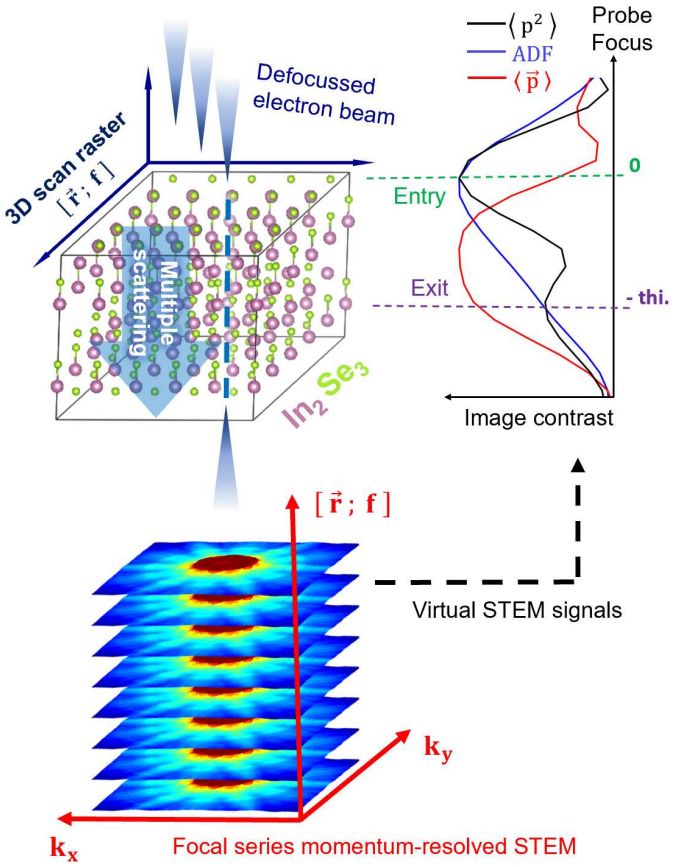

Figure 2: Experimental set-up (schematic) for focal-series 4D STEM employed in this work. The α-In_2Se_3 crystal is depicted, as well as the 3D scan scheme performed in real-space. Following the complex interaction of the high-energy electrons with the crystal involving, e.g., multiple scattering, diffraction patterns are recorded as a function of the coordinate within the 3D scan $[\vec{r};f]$, where $\vec{r}$ is the 2D scan position and f is the probe focus. Virtual STEM signals are then extracted as a function of focus. The contrasts extracted for each signal display a specific focus-dependence, which can be related to the specimen geometry, e.g. the vertical positions of its interfaces with vacuum.

1.2. Simulation details

A comprehensive simulation study was performed using the multislice algorithm [36] to include multiple scattering and propagation. Given the rather large lattice parameter a_c=1.92 nm, each unit cell was divided into four slices. Furthermore, as the electron wave broadens significantly in real space by focus, scattering and propagation, we generated a supercell with a lateral extension of 9×5 Bravais cells which corresponds to a size of 3.62× 3.48 nm. Crystallographic tilt from the major beam incidence [001] was accounted for by a modified Fresnel propagator. Diffuse scattering arising from thermal vibrations of the lattice was included via the frozen phonon approximation [37], assuming uncorrelated thermal vibrations according to the Einstein model. In this instance, we found that a total number of 15 phonon configurations was sufficient to converge the signals of interest. Isotropic mean-squared displacements of $\langle u^2_{\mathrm{In}}\rangle = 0.0114\,\text{Å}^2$ and $\langle u^2_{\mathrm{Se}}\rangle = 0.0101\,\text{Å}^2$ were used for In and Se atoms, respectively. The sampling in the simulations was chosen in accordance with experimental settings, that is, a scan step of 31 pm and a focus step of 1.5 nm. The spatial frequency cut-off was set to approximately 186 nm^{-1}.

2. Focal series momentum-resolved STEM experiments

2.1. Brief survey of relevant STEM signals

Signals of interest were extracted from the diffraction patterns by application of virtual STEM detectors, as depicted in Fig. 3. Whereas the geometry of the detectors represented by binary masks has formerly been predetermined by hardware, rings and discs with flexible geometry can be defined for evaluating bright field (BF), annular bright field (ABF) or annular dark field (ADF) signals. Besides the flexibility provided by the 4D data set, we can also correct for the elliptical distortion owing to the microscope's projection system. In that way, we associate each pixel in the recorded diffraction pattern to an accurately known spatial frequency $\vec{k} = [\,kx\,;\,k_y\,]$, corresponding to a momentum $\vec{p} = h\vec{k}$, with h the Planck constant. This metric was used to determine all virtual detectors depicted in Fig. 3, i.e. for the binary masks as well as for the calculation of first and second moments. Note that the relative rotation between the axes in real and reciprocal space, itself being caused by a rotation between the scan axes and the camera, is accounted for as well. In the following, we summarise the characteristics of each signal briefly.

Bright field (BF). Bright field detectors integrate intensity over a usually disc-shaped region within the Ronchigram, being the complex interference pattern formed by the undiffracted beam and the diffracted beams. The BF signal is, to a large extent, determined by elastic scattering and is additionally sensitive to aberrations of the probe-forming lens. Following the principle of reciprocity [38], BF contrast is analogous to imaging in conventional,

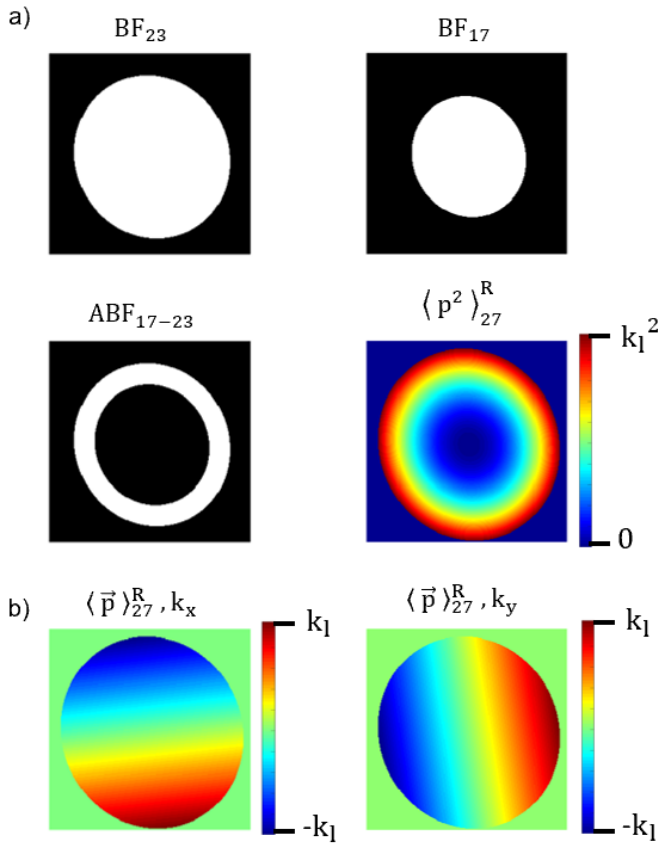

Figure 3: Virtual detectors used to generate the images. In b) the two components of the vector-valued detector employed for the first moment calculation are depicted. All other detectors are given in a).

plane-wave-illumination TEM, with a degree of partial spatial coherence given by the size of the BF detector. Features such as contrast reversal in dependence of focus and specimen thickness are therefore observed in BF-STEM. Here we employ two distinct bright field signals, BF_{23} and BF_{17}, indicating detector radii of 23 mrad (meaning the full primary beam), and 17 mrad, respectively.

Annular bright field (ABF). The signal is formed by the summation of intensity within an annular region inside the BF region. Whereas the outer radius is typically close to the radius of the primary beam, the inner one usually covers 50 to 80 % of it. This imaging mode is most commonly employed to obtain high contrast of both light and heavy atoms in the specimen simultaneously. It is, however, very sensitive to dynamical scattering, aberrations [29, 30] and crystal orientation [39]. Overall, ABF is not only an alternative to BF imaging [40], but also a complement to the HAADF mode. In this work, the ABF_{17-23} signal is obtained by summing intensity scattered at angles comprised between 17 and 23 mrad. It is therefore equal to the difference between the BF_{23} and BF_{17} signals.

First moment. By using momentum-resolution, the vectorial first moment of each diffraction pattern could recently be put into practice in STEM [19]. The kernel of the computation is the sum over all two-dimensional spatial frequency vectors $\vec{k}$ in the diffraction pattern, sampled via the pixels of an ultrafast camera, with each summand being weighted by the local scattered intensity. In practice, this summation can only be carried out up to a cut-off scattering angle θ_l, corresponding to a spatial frequency $k_l = \lambda^{-1} \sin\theta_l$, with λ the electron wavelength. Previous studies [41], however, have shown that the first moment converges quickly with θ_l being larger than the Ronchigram radius. Importantly, the first moment of a normalised distribution can be identified as $\langle\vec{p}\rangle$, the average momentum transferred to the probe by the interaction with the specimen. This, in turn, can be used to measure subatomic and polarisation-induced electric fields under certain conditions [19, 21]. Understanding the dependence of $\langle\vec{p}\rangle$ on focus and scattering dynamics is therefore highly relevant for both fundamental physics and the electrical characterisation of materials. For the present purposes, we indicate the cut-off angle θ_l as a subscript to $\langle\vec{p}\rangle$ and use superscripts R and N to distinguish between the raw summation

$$\langle\vec{p}\rangle^{\mathrm{R}}_{\theta_l}(\vec{r}) = \sum_{k<k_l} \vec{k} I(\vec{r};\vec{k}) \tag{1}$$

and the normalised case

$$\langle\vec{p}\rangle^{\mathrm{N}}_{\theta_l}(\vec{r}) = \frac{\langle\vec{p}\rangle^{\mathrm{R}}_{\theta_l}(\vec{r})}{\sum\limits_{k<k_l} I(\vec{r};\vec{k})} \quad , \tag{2}$$

with $I(\vec{r};\vec{k})$ the intensity scattered to the spatial frequency $\vec{k}$ at the scan position $\vec{r}$. In the present study, each diffraction pattern was multiplied by two masks presented in Figs. 3 b, corresponding to the axes $[k_x;k_y]$, followed by a

summation over all entries to calculate $\langle\vec{p}\rangle^{\mathrm{R}}_{27}$. Note that the $\vec{k}$-space coordinate system has been aligned with that of the scan, leading to a slight rotation as depicted in Fig. 3 b.

Second moment. The scalar quantity $(\mu_{20}+\mu_{02}) = \langle p^2\rangle$ is obtained by summing the diffracted intensity while weighting each summand with the square modulus of the respective spatial frequency. In analogy to eqs. (1,2) this reads

$$\langle p^2\rangle^{\mathrm{R}}_{\theta_l}(\vec{r}) = \sum_{k<k_l} k^2 I(\vec{r};\vec{k}) \tag{3}$$

for the raw summation and

$$\langle p^2\rangle^{\mathrm{N}}_{\theta_l}(\vec{r}) = \frac{\langle p^2\rangle^{\mathrm{R}}_{\theta_l}(\vec{r})}{\sum\limits_{k<k_l} I(\vec{r};\vec{k})} \tag{4}$$

for the normalised case respectively. The mask to calculate $\langle p^2\rangle^{\mathrm{R}}_{\theta_l}$ applied to each diffraction pattern before summing is depicted in Fig. 3 a bottom right. Similarly to considerations in conjunction with the lateral momentum transfer $\langle\vec{p}\rangle^{\mathrm{N}}_{\theta_l}$, one tends to identify $\langle p^2\rangle^{\mathrm{N}}_{\theta_l}$ with the expectation value of the lateral kinetic energy. This becomes obvious when replacing $I(\vec{r},\vec{k})$ by the squared modulus of the wave function and performing a transition from summation to continuous integration. However, $\langle p^2\rangle^{\mathrm{N}}_{\theta_l}(\vec{r})$ does not necessarily converge with increasing θ_l, contrary to $\langle\vec{p}\rangle^{\mathrm{N}}_{\theta_l}$. In particular, the scattering of electrons with opposite momentum transfer cannot cancel out. Whether eq. (4) converges with increasing θ_l or not is therefore determined by the characteristics of $I(\vec{r},\vec{k})$ for $k\to\infty$. A study of convergence will hence be presented both analytically and by simulations below. For reasons of simplicity, this quantity will be further referred to as the second moment, though this term conventionally refers to the wider definition $\mu_{ij} = \sum k_x^i k_y^j I(\vec{k})$, with $i+j=2$.

Annular dark field (ADF). This signal is formed by integrating the scattered intensity over a ring-shaped detector. The most convenient configuration is high-angle ADF (HAADF) where detector acceptance angles are between several tens and hundreds of milliradians, which leads to a dominating thermal diffuse scattering (TDS) contribution. The HAADF imaging mode furthermore displays high sensitivity to specimen thickness and chemical composition [42–45], often referred to as Z-contrast. In low-angle ADF (LAADF), TDS and Bragg scattering are both present, which has been shown to reveal contrast of buried interfaces [46].

MR-STEM. In this work, the central part of the diffraction pattern is recorded with resolution in $\vec{k}$-space. This is thus a four-dimensional imaging mode, as a two-dimensional diffraction pattern is assigned to each position of a two-dimensional scan. Due to the availability of a large range of spatial frequencies, this method can be employed to generate all aforementioned contrasts post-experiment, in the limit of available $\vec{k}$ coordinates. In that regard, we combined the MR-STEM acquisition with a dedicated HAADF detector covering 39 to 230 mrad, in order to explore scattering beyond the region covered by the fast camera at least in terms of its annular integral.

2.2. Experimental results

Figure 4 compiles signals generated from the FS-MR-STEM acquisition of In_2Se_3 within a focal range of 30 nm in total. For each signal, scans taken at different foci are aligned horizontally with the focus increasing from left to right. The field of view covers a square region of approximately 4 nm^2 as indicated. To go further, the first moment $\langle\vec{p}\rangle^{\mathrm{N}}_{\theta_l}$, due to its sensitivity to electric fields, usually comes along with the divergence map ρ_{θ_l}, being proportional to the charge density, and the integral map ϕ_{θ_l}, being proportional to the electrostatic potential in thin specimen. ρ_{θ_l} and ϕ_{θ_l} are given by

$$\rho_{\theta_l}(\vec{r}) = \vec{\nabla}_\perp . \langle\vec{p}\rangle^{\mathrm{N}}_{\theta_l}(\vec{r}) \tag{5}$$

and

$$\langle\vec{p}\rangle^{\mathrm{N}}_{\theta_l}(\vec{r}) = \vec{\nabla}_\perp \phi_{\theta_l}(\vec{r}) \quad . \tag{6}$$

In this work, ϕ_{θ_l} is obtained from ρ_{θ_l} by solving the Laplacian $\vec{\nabla}^2_\perp \phi_{\theta_l} = \rho_{\theta_l}$ iteratively using a five-point-stencil numerical integration scheme based on finite differences. The details of the method are given in appendix B.

Figure 5 displays the standard deviation σ as a measure of contrast, calculated from each respective signal, in dependence of focus. This calculation is done after drift correction based on cross-correlating subsequent HAADF images, such that the contrast is evaluated within a region common to each subsequent recording. For reasons of clarity, each curve is plotted between its minimum and maximum values. Local maxima are marked in Fig. 4 as red squares around the respective images. In the particular case of $\langle\vec{p}\rangle^{\mathrm{R}}_{27}$ and $\langle\vec{p}\rangle^{\mathrm{N}}_{27}$, the calculation of σ has to be done from a selected scalar quantity, derived from the vectorial quantity. Here, we employ the divergence ρ_{27}, as it allows the atomic information contained in the first moment to be displayed clearly and reliably.

Before going into the details of the individual images, two observations are made immediately. First, all signals vary significantly within the focal range covered here. Second, and most importantly, the signals exhibit an individual dependence of contrast on probe focus. This is remarkable since it has important practical consequences, in addition to implications of focal dependencies found, e.g., for segmented ABF scattering in earlier works [32]. In particular, with the locations of the local contrast maxima being highlighted, Fig. 4 shows that, though MR-STEM can be used to generate many different signals carrying different types of information on momentum transfer (location of light and heavy atoms etc.), a single acquisition is incapable of providing all signals with the highest achievable contrast and interpretability. In fact, this relativises the common attitude tending to consider MR-STEM a universal imaging mode. Furthermore, as the signals contain possess differing dependences to different physical parameters,

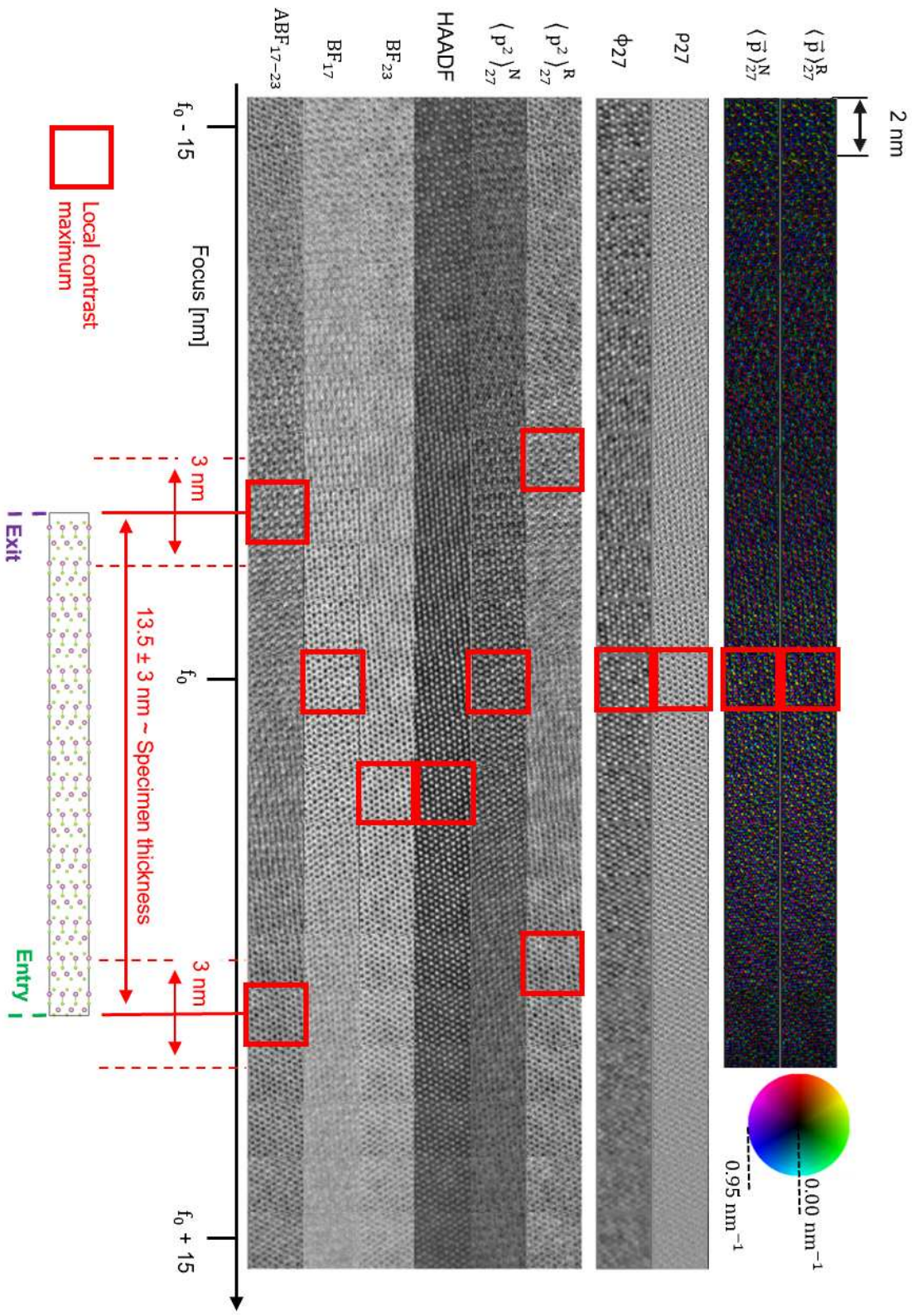

Figure 4: The experimental images calculated for each focus coordinate. The size of the field of view is equal to 2 nm. The images displaying contrast optima are highlighted in red. The vectorial quantities $\langle \vec{p} \rangle^{R}_{27}$ and $\langle \vec{p} \rangle^{N}_{27}$ are given in colour wheel representation, with the modulus being depicted as well. Note that the minimum and maximum moduli taken by the vectors, as indicated on the legend, is given for $\langle \vec{p} \rangle^{N}_{27}$, and not $\langle \vec{p} \rangle^{R}_{27}$, due to the latter being dependent on intensity values, contrary to the former. The specimen, with its interfaces with vacuum, is depicted below the images.

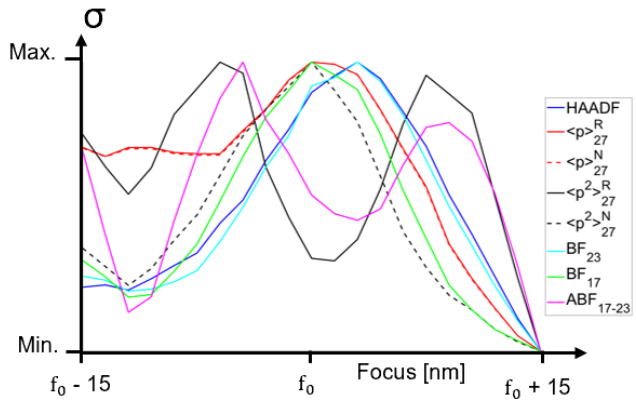

Figure 5: Standard deviation σ plotted against focus for all signals of interest. In the case of the vectorial quantities $\langle\vec{p}\rangle^{\mathrm{R}}_{27}$ and $\langle\vec{p}\rangle^{\mathrm{N}}_{27}$, σ is calculated from the divergence. Each curve is scaled between its minimum and maximum.

an in-depth evaluation of the focus-dependent contrast of different signals is expected to shed light on additional characteristics of the specimen and scattering physics.

A closer look into Fig. 4 reveals that the maximally localized average deflections of the incident probe, as mapped by the vector fields $\langle\vec{p}\rangle^{\mathrm{R,N}}$, occur at a slightly lower focus than the HAADF signal, the difference being approximately 3 nm (two focus steps) here. In other words, highest sensitivity to atomic electric fields, although being related to $\langle\vec{p}\rangle^{\mathrm{N}}$ in non-linear manner for elevated thickness through dynamical scattering, is obtained for a different incident wave than the one needed to reach the highest sensitivity to chemical composition.

The orientation of $\langle\vec{p}\rangle^{\mathrm{N}}_{27}$ is shown in more detail in Fig. 6, where the vector field obtained at the focus of maximum contrast is displayed, alongside the corresponding BF_{23} result and the two byproducts ρ_{27} and ϕ_{27}. The first moment vectors point towards the atomic positions detected in the bright field image which is consistent with the electrons being attracted by the partially unscreened positive charge of the atomic nuclei. As a consequence, the atomic columns appear as local minima of ρ_{27}.

Going back to Fig. 4, a feature observed for both the ABF_{17-23} and $\langle p^2\rangle^{\mathrm{R}}_{27}$ series is the occurrence of two contrast maxima with opposite contrast, i.e., one with maxima and one with minima at the atomic sites. This becomes evident by comparing with the HAADF signal. All other signals only exhibit one contrast maximum located in between those of ABF_{17-23} and $\langle p^2\rangle^{\mathrm{R}}_{27}$. Interestingly, HAADF and BF_{23} share the same optimum, whereas the one found for BF_{17} is located at a 3 nm lower focus. On the one hand, this shows the importance of the outer bright field acceptance angle in defining the dependence to focus, on the other hand the images of the $\mathrm{In_2Se_3}$ crystal lattice differ for the two BF signals at the foci of maximum contrast. Note that this focus doesn't necessarily need to be the preferable setting for, e.g., reliable structural imaging

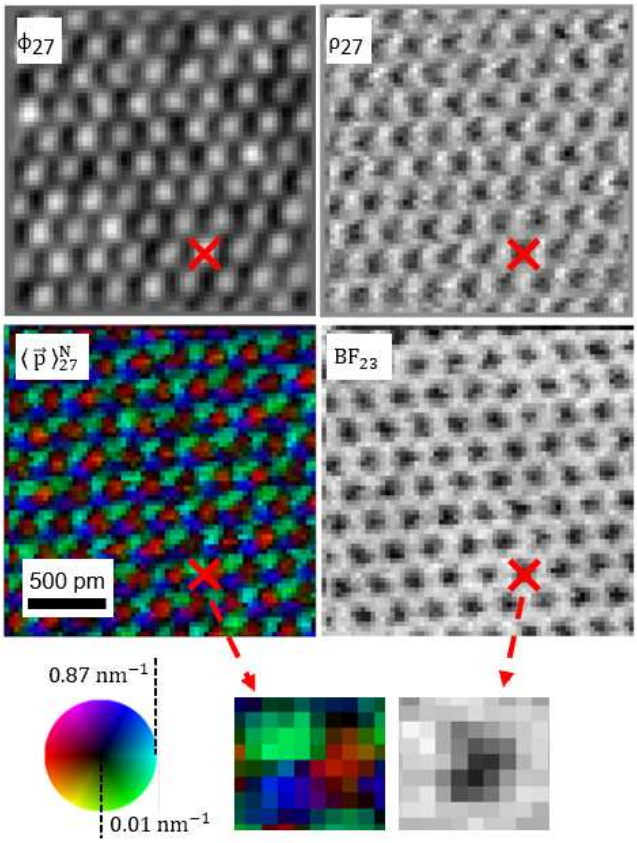

Figure 6: The $\langle\vec{p}\rangle^{\mathrm{N}}_{27}$ vector field, at its focus of maximum contrast, is displayed alongside its divergence and integral. The BF_{23} counterpart is depicted as well. A subset of the images is shown containing the expected atomic pattern, meaning a set of first moment vectors pointing toward the atomic site.

where local extrema of the signals need to coincide with the positions of the atoms.

Regarding the 4D STEM-specific signals, the $\langle\vec{p}\rangle^{\mathrm{R}}_{27}$ and $\langle\vec{p}\rangle^{\mathrm{N}}_{27}$ signals exhibit an identical behavior, showing the convergence of the signal, even for a cut-off angle as low as 27 mrad. This is different from $\langle p^2\rangle^{\mathrm{R}}_{27}$, whose focus-dependence differs strongly from its normalized counterpart, as $\langle p^2\rangle^{\mathrm{N}}_{27}$ only shows one contrast maximum coinciding with BF_{17} and the first moment.

As to the signals for which two distinct contrast optima occur, the implication is that at least one of those corresponds to the scanning process being performed with a non-minimal extension of the electron probe in real space. This appears counterintuitive, because most of the literature on high-resolution STEM assumes an atomically sharp probe as a requirement for reaching atomic contrast. Similar features have been outlined in simulations of LAADF imaging [46], where maxima of peak intensity were found at foci coinciding with the vertical position of interfaces between layers of different materials, and with vacuum. Here, the contrast maxima for both $\langle p^2\rangle^{\mathrm{R}}_{27}$ and ABF_{17-23} are approximately nine focus steps of 1.5 nm each apart, which coincides well with the measured specimen thickness. This observation leads to an interpretation where the vertical positions of the specimen's entrance and exit surfaces indeed correspond to these two contrast maxima. Evaluating FS-MR-STEM would then provide a way to probe the entrance and exit face geometry experimentally, while simultaneously yielding information on chemical composition and/or electric fields. Moreover, further elucidating why focusing the probe at the exit face yields maximum image contrast, irrespectively of dynamical scattering, is interesting from the standpoint of fundamental physics as well. In order to clarify the focus-dependencies, establish potential relationships to the specimen geometry, and to study the dependence on thickness, we pursue by comprehensive dynamical simulation studies.

3. Theoretical considerations

3.1. Simulation studies

The signals dealt with in the experimental section have been simulated for several specimen thicknesses and probe foci, as depicted in Fig. 7 for conventional detector geometries, and in Fig. 8 for signals explicitly employing momentum resolution. The standard deviation σ was calculated within one unit cell for each thickness and foci, and plotted in Fig. 9. Because the main interest lies in the contrast variations induced by the focus, σ has been scaled between its minimum and maximum values within a focal series at a given thickness. The simulations include the experimental crystallographic tilt of 1.7 mrad, and no other aberrations than probe focus. A low-angle annular dark field signal, LAADF_{23-29}, which is not experimentally available due to the high camera length used for the recording, is simulated as well for completeness. The vertical locations of both entrance and exit surfaces on the focus axis, alongside the experimentally measured thickness, are indicated in order to facilitate the interpretation as to geometric features.

The bright field signals $\mathrm{BF}_{23,17}$, seen in Fig. 7 a,b, exhibit rich contrast features depending on detector angles, focus and thickness in rather complex manner, which is typical for conventional TEM imaging. Foci that geometrically lie inside the specimen are leading to negative contrast, being consistent with the experimental results shown in Fig. 4. Whereas the contrast of BF_{23} changes weakly with focus, BF_{17} shows a significantly sharper contrast maximum shifted closely to the exit face.

The $\mathrm{ABF}_{17-23} = \mathrm{BF}_{23} - \mathrm{BF}_{17}$ signal, in Fig. 7 c, shows high contrast at the specimen surfaces as a systematic feature. This is in agreement with the experimental ABF signal presented in Fig. 4 as well, including the observed negative to positive contrast change when focusing through the specimen from the entry to the exit face. A further observation is the existence of additional, smaller, contrast maxima at foci a few nanometers above and below the surfaces. Contrary to the BF_{23} and HAADF signals, the ABF_{17-23} contrast maxima appear to be very sharp along the focus dimension, with minimum contrast obtained in between the two surfaces.

Low-angle scattering, assessed by the LAADF_{23-29} signal, in Fig. 7 d, exhibits a pronounced maximum for foci close to the exit face, and another one at the entrance, for thicknesses above 10 nm. No contrast reversal is observed along the focus dimension. Note that, similarly to ABF_{17-23}, the behavior is very dependent on the exact acceptance angles [46]. Considerable high-angle contrast, as shown by the HAADF signal, in Fig. 7 e, occurs for foci between entrance and exit face. A broad positive contrast maximum is found at foci a few nanometres below the surface, which is consistent with both our experimental results for a thickness of 13.45 nm, and previous work from Beyer et. al. [48].

As shown in Fig. 8 a, the average momentum transfer $\langle\vec{p}\rangle^{\mathrm{N}}_{27}$ reaches its contrast maximum when focusing into the bulk specimen, with a tendency to follow the exit face for thicknesses below 8 nm. Remarkably, above this thickness, the focus-dependence neither follows the bright nor the dark field characteristics, as the maximum contrast is then found at a constant depth below the entrance surface, independently of the distance to the exit surface. Consequently, for sufficiently large thicknesses, this must be kept in mind when accessing, e.g., electric fields and chemical composition using a single simultaneous acquisition of $\langle\vec{p}\rangle^{\mathrm{N}}_{27}$ and HAADF, since the foci of maximum contrast differ systematically. Additionally, the focus- and thickness-dependence observed for the quantities ρ_{27} and ϕ_{27}, depicted in Fig. 8 b,c, follows the same pattern as the one of $\langle\vec{p}\rangle^{\mathrm{N}}_{27}$.

At the contrast maximum of $\langle\vec{p}\rangle^{\mathrm{N}}_{27}$, atoms appear as sinks of momentum transfer, such that the vectors point towards the atomic sites. This is depicted in Fig. 10 a, where the vector field $\langle\vec{p}\rangle^{\mathrm{N}}_{27}$ is shown for the experimental thickness of 13.45 nm, at the focus of maximum contrast,

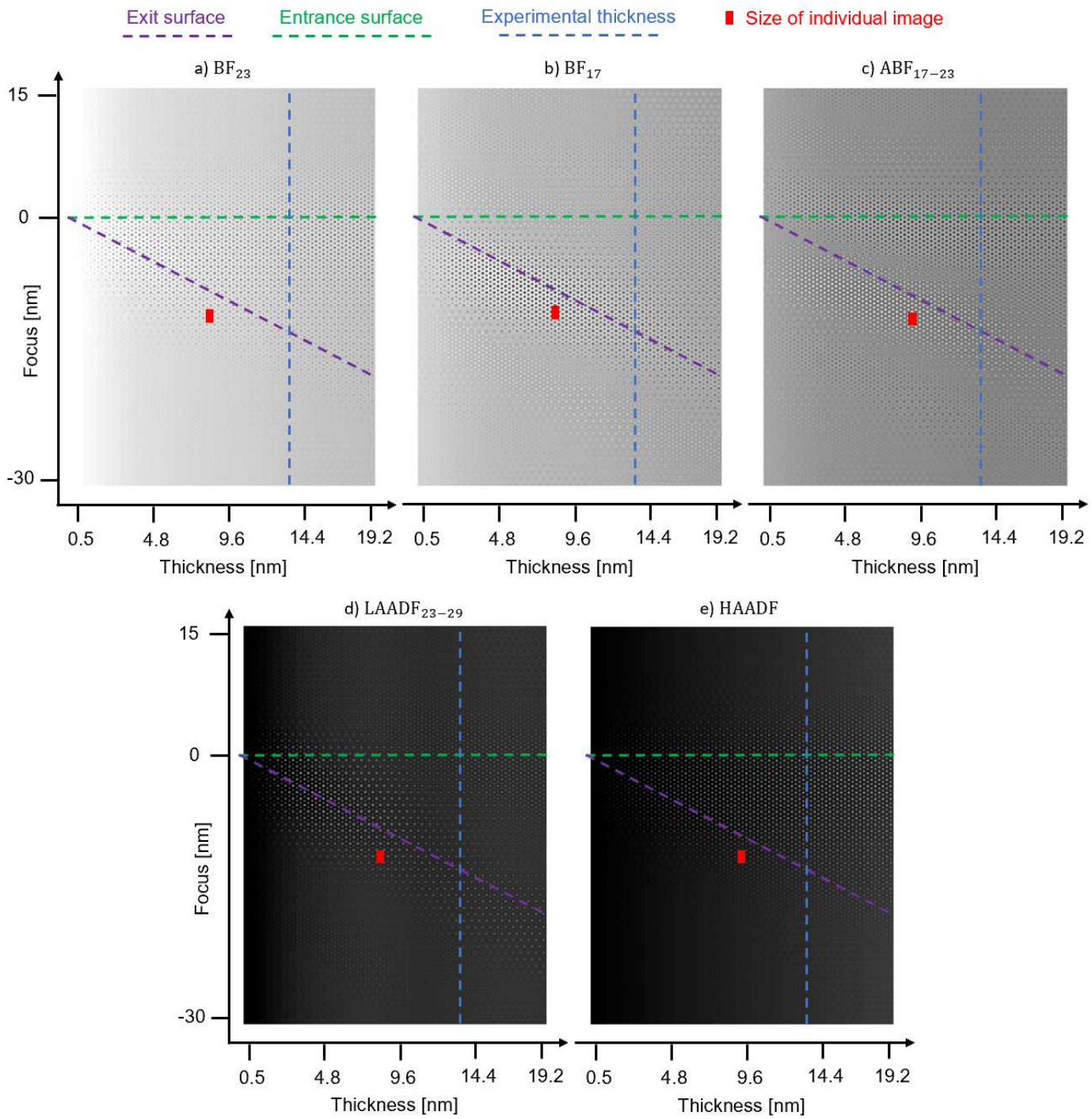

Figure 7: Conventional STEM signals extracted from the simulation. Data is given as a function of specimen thickness and probe focus, the latter being zero at the entrance surface. The positions of the entrance and exit surfaces on the focus axis are indicated as well. The size of an single scanned image in the graph is indicated as a red rectangle.

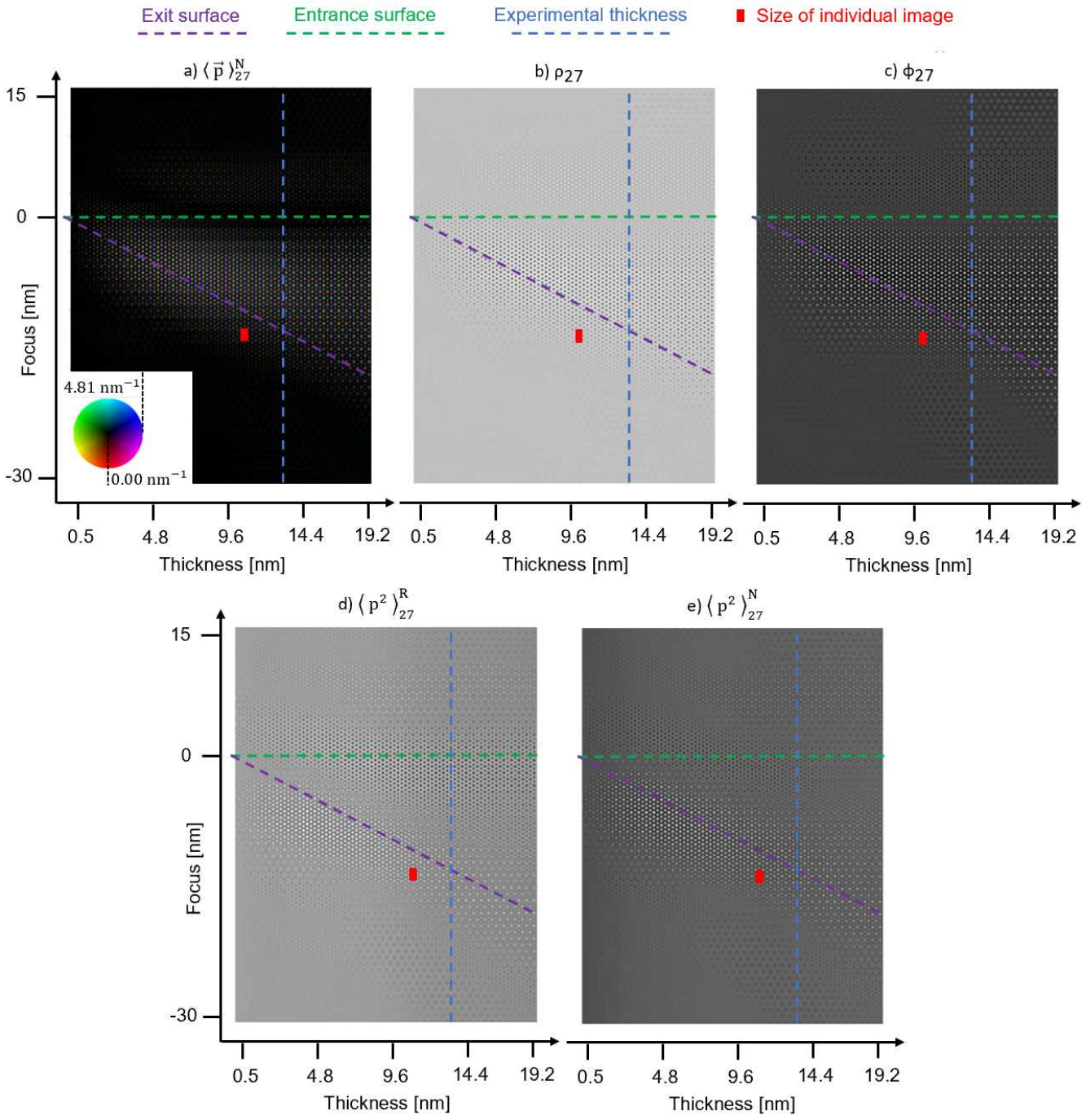

Figure 8: 4D STEM-specific signals, including $\langle \vec{p} \rangle^{N}_{27}$, $\langle p^2 \rangle^{R}_{27}$ and $\langle p^2 \rangle^{N}_{27}$. Vectorial quantities are given using a colour wheel representation. Data is given as a function of specimen thickness and probe focus, the latter being zero at the entrance surface. The positions of the entrance and exit surfaces on the focus axis are indicated as well. The size of a single image in the graph is indicated as a red rectangle.

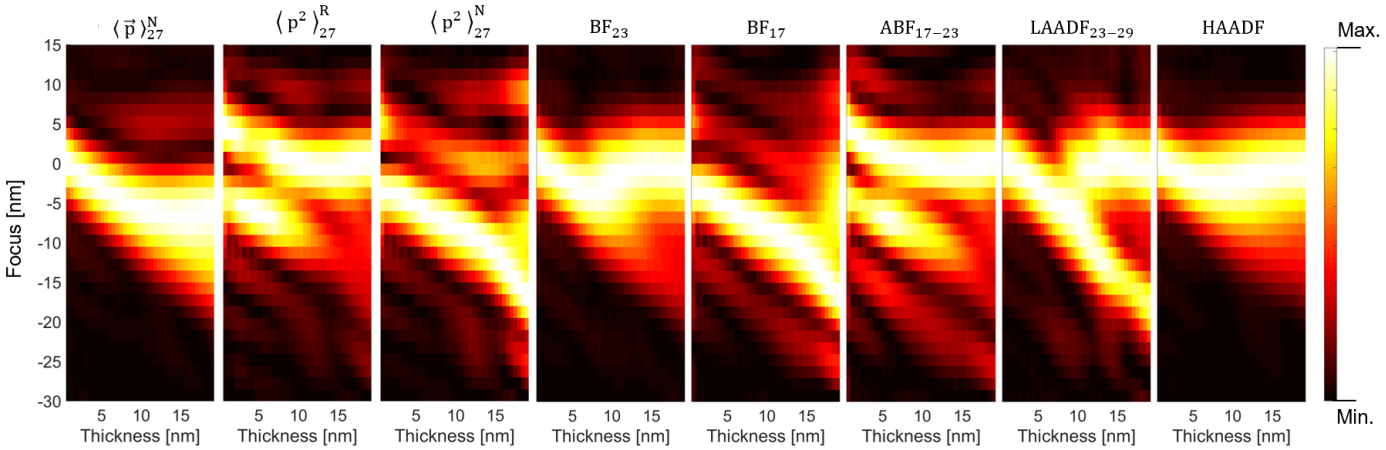

Figure 9: Contrast profiles extracted from the signals displayed in figures 7 and 8. σ is given scaled between its minimum and maximum value alongside the focus dimension, for each given thickness, meaning that the values are normalized to minimum and maximum at the level of each column in the graph. As in Fig. 5, σ, for the quantity $\langle \vec{p} \rangle^{N}_{27}$, is obtained from its divergence.

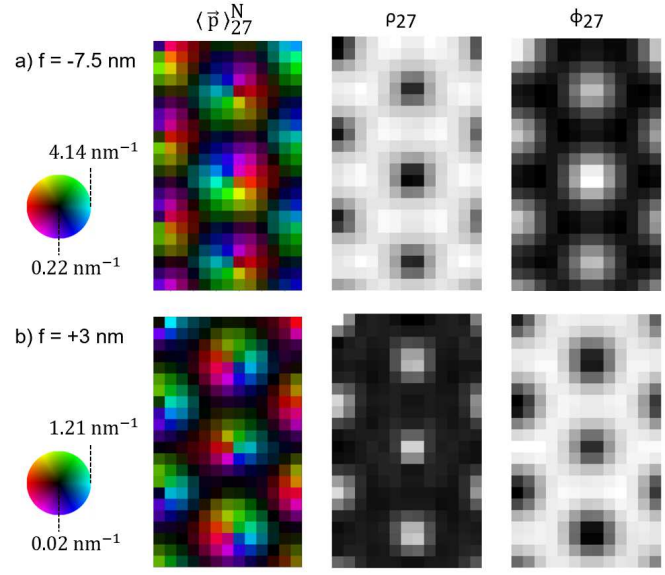

Figure 10: The simulated $\langle \vec{p} \rangle^{N}_{27}$ image for a thickness of 13.45 nm, and a focus of a) -7.5 nm and b) +3 nm. The vectors are depicted using the colour wheel representation. The integral and divergence of the vector fields is depicted as well.

alongside ρ_{27}, which displays local minima at the atomic positions, and ϕ_{27}. Those observations are, as in the experimental case, consistent with the intuitive physical interpretation under which the electrons are attracted by the positive charge carried by the atomic nuclei, which therefore induces a shift in the center of mass of the diffraction pattern towards the atomic column [19, 20, 41]. However, although the contrast is fairly low at foci close to the top surface, a faint contrast maximum is observed above it. Interestingly, the momentum transfer vectors are then pointing away from the atomic sites, now being sources rather than sinks of momentum transfer as depicted in Fig. 10 b. Whereas the mismatch of optimum foci between $\langle \vec{p} \rangle^{N}_{27}$, HAADF and BF is confirmed experimentally in Fig. 4, this sign change of for foci above the entrance surface $\langle \vec{p} \rangle^{N}_{27}$ is difficult to see in the experimental vector field due to counting statistics.

For the $\langle p^2 \rangle^{R}_{27}$ signal, presented in Fig. 8 d, we find two focus optima with negative and positive atom contrast at the entrance and exit faces, respectively, which is also consistent with the experimental results. In particular, significant similarity to the ABF_{17-23} behaviour is observed. Nevertheless, the analysis of $\langle p^2 \rangle^{R}_{\theta_l}$ as a function of cut-off angle θ_l shows high robustness of the surface sensitivity, whereas ABF and LAADF contrasts depend critically on the choice of scattering angles covered by the (virtual) detector. The normalized counterpart $\langle p^2 \rangle^{N}_{27}$, in Fig. 8 e, shows a similar focus-dependence with increased contrast close to the exit surface.

Whereas convergence and physical meaning of $\langle \vec{p} \rangle^{R,N}_{\theta_l}$ have been deciphered in earlier work [41], we now address the behaviour of $\langle p^2 \rangle^{R,N}_{\theta_l}$ when including higher-angle contributions.

3.2. High-angle characteristics of the second moment $\langle p^2 \rangle$

3.2.1. Variation of focus-dependence for increasing cut-off angle

The focus-dependence of the $\langle p^2 \rangle^{\mathrm{R}}$ and $\langle p^2 \rangle^{\mathrm{N}}$ signals was found to be inherently thickness-dependent, with two contrast maxima found at the vertical location of interfaces with vacuum. It is, however, relevant to assess the robustness of these findings to variations of the cut-off angle, as well as to investigate the effect of including contributions from larger scattering angles to those signals.

In Fig. 11, the second moment is given as a function of thickness and focus for a selection of cut-off angles, each separated from the previous value of 27 mrad by a multiple of 16 mrad. We thus show the signals obtained with a cut-off of 43 mrad, in Fig. 11 a,d, 59 mrad, in Fig. 11 b,e and 75 mrad, in Fig. 11 c,f. The raw quantity $\langle p^2 \rangle^{\mathrm{R}}_{\theta_l}$ is depicted in Fig. 11 a,b,c and the normalized counterpart $\langle p^2 \rangle^{\mathrm{N}}_{\theta_l}$ in Fig. 11 d,e,f.

As can be observed immediately, the two contrast maxima are still present, though faintly in Fig. 11 a,d. This is remarkable because it demonstrates the conservation of surface sensitivity for a large range of cut-off angles, up to values above 40 mrad. As a consequence, surface detection through the use of the second moment is shown to be possible with robustness against variations of this parameter.

For the two further cases studied, 59 mrad and 75 mrad, we observe a transition toward new focus-dependencies, having similarities with the ADF imaging modes presented in Fig. 7 d,e. The contrast is then seen to remain positive, with local maxima coinciding with the positions of atomic columns. In the 59 mrad case in Fig. 11 b,e, the contrast is found to be higher close to the exit face, while, in the 75 mrad case in Fig. 11 c,f, the contrast goes through a smooth decay across specimen thickness, with a peak close to the entrance face. These findings can be related to the weighting being equal to the square of the spatial frequency, thus leading to a stronger impact of high-angle contributions relative to those of lower scattering angles.

To go further, it is noteworthy that the difference between the raw and normalised second moment $\langle p^2 \rangle_{\theta_l}$ of the scattered intensity has its origin in the finite cut-off angle, which is unavoidable given the finite solid angle that can be covered by the camera. When the electron probe is positioned on an atomic column, high-angle scattering beyond this cut-off increases as compared to positions in between, such that the denominator of eq. (4) varies with the probe position whenever the summation does not include the total scattered intensity.

In order to assess the thickness dependence in conditions where the high-angle contribution becomes dominant, we plot the value taken by the real-space average of $\langle p^2 \rangle^{\mathrm{N}}_{\theta_l}$ against specimen thickness in Fig. 12. The measurement is done for increasing values of cut-off angle θ_l, over a new set of multislice simulations, this time performed in exact [001] zone axis geometry, with a fixed focus of 0 nm and an increased spatial frequency cut-off of about $373\,\mathrm{nm}^{-1}$, thus allowing to reproduce diffraction features at higher angles. Results display a monotonous variation of $\langle p^2 \rangle^{\mathrm{N}}_{\theta_l}$ against increments of specimen thickness, similarly to observations made about the ADF mode in past work [42, 43].

3.2.2. Analytical treatment by Mott scattering

Relativistic electron scattering in solids is a complex function of the detailed arrangement of atoms with respect to a given incident beam direction, as well as the details of the incident electron wave function. Whereas extensive numerical multislice [36] or Bloch wave [49] simulations are needed to calculate the angular distribution of scattered electrons quantitatively, simplified and abstract analytical considerations need to be employed to shed light on global aspects of the scattered intensity [50, 51]. Here, we are interested in the convergence of $\langle p^2 \rangle_{\theta_l}$ for θ_l going towards infinity, which is thus dominated by high-angle scattering. Unlike Bragg scattering at low and medium angles, scattering to high angles is largely incoherent with respect to the actual atomic structure. This means that, at least in the case where $\theta_l \to \infty$, we can regard the scattered intensity as being the incoherent summation over single atom scattering events. Hence, it is sufficient to consider electron scattering at a single atom to obtain the main characteristics of $\langle p^2 \rangle_{\theta_l}$ for large cut-offs θ_l.

The atomic scattering potential is produced by the sum of the nuclear charge density $e\rho_Z(\vec{R})$ of a nucleus with atomic number Z and elementary charge e, and the electronic charge density $-e\rho_X(\vec{R})$. Note that we use capital letters $\vec{R}$ and $\vec{K}$ for the three-dimensional real and reciprocal space, respectively, to distinguish from the two-dimensional vectors $\vec{r}$ and $\vec{k}$ considered in the previous sections. By employing the Poisson equation and assuming a point-shaped nucleus represented by Dirac's delta function with $\rho_Z(\vec{R}) = Z\delta(\vec{R})$, the Mott-Bethe relation is obtained, which relates the atomic scattering amplitudes f^e and f^X for electrons and X-rays, respectively,

$$f^e(\vec{K}) = \frac{e}{4\pi^2\varepsilon_0\vec{K}^2}\left[Z - f^X(\vec{K})\right] \approx \frac{Ze}{4\pi^2\varepsilon_0\vec{K}^2} \quad . \qquad (7)$$

The approximation is only valid for high-angle scattering for which electrons interact dominantly with the unscreened nuclear potential, such that f^X, being the Fourier transform of the electronic charge density, can be neglected.

The incident electrons interact with the projected potential of the atom if we consider only single scattering. Because $f^e(\vec{K})$ is the Fourier transform of the atomic Coulomb potential, $f^e(\vec{k})$ is the Fourier transformed potential projected along z-direction.

The limit of $\langle p^2 \rangle_{\theta_l}$ for increasing θ_l will not depend on the details of the illumination. Let us, therefore, assume plane wave incidence. Note that this doesn't contradict the observed focus dependence in the previous part, because we now let $\theta_l \to \infty$, which, as demonstrated in the previous subsection, leads to a domination of the high-angle

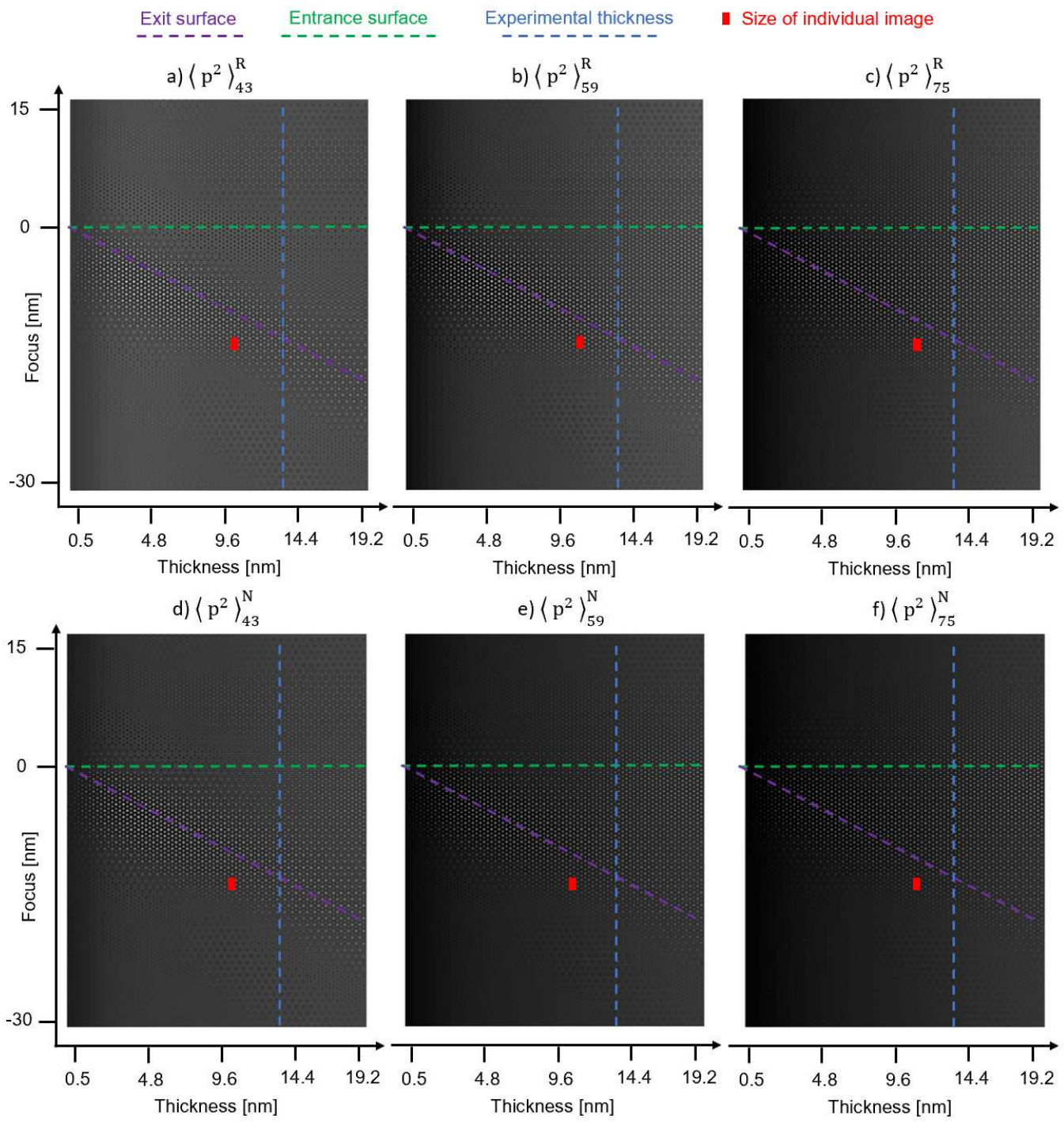

Figure 11: $\langle p^2 \rangle^{\mathrm{R}}_{\theta_l}$ and $\langle p^2 \rangle^{\mathrm{N}}_{\theta_l}$ signals for increasing cut-off angles θ_l. Data is given as a function of specimen thickness and probe focus, the latter being zero at the entrance surface. The positions of the entrance and exit surfaces on the focus axis are indicated as well. The size of an single image in the graph is indicated as a red rectangle.

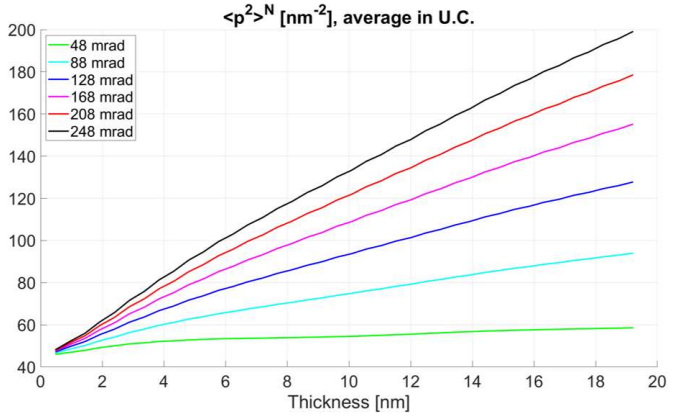

Figure 12: Result of the real-space average of $\langle p^2 \rangle^{\mathrm{N}}_{\theta_l}$ images, within one unit cell, for increasing specimen thickness. The measurement was done with varying cut-off angle θ_l. $\langle p^2 \rangle^{\mathrm{N}}_{\theta_l}$ is expressed in nm^{-2}.

contribution. The scattered intensity is then proportional to

$$I(\vec{k}) = \frac{Z^2 e^2}{16\pi^4 \varepsilon_0^2 \vec{k}^4} =: \frac{C_1}{\vec{k}^4} \quad . \tag{8}$$

The integration of just $I(\vec{k})$ over ring segments $k\mathrm{d}\varphi\,\mathrm{d}k$ in the diffraction pattern up to a cut-off k_l directly yields the hyperbolic convergence to the total intensity as $-k_l^{-2}$.

For the second moment, we have:

$$\begin{aligned} \langle k^2 \rangle_{\theta_l} &= C_0 + 2\pi C_1 \int_{k_m}^{k_l} \frac{1}{k^4} \cdot k^2 \; k \,\mathrm{d}k \\ &= C_0 + 2\pi C_1 \log\left(\frac{k_l}{k_m}\right) \end{aligned} \tag{9}$$

where we introduced the lower integration limit $k_m > 0$. This is justified since eq. (8) is an approximation for high-angle scattering. For lower angles, f^X would need to be taken into account to avoid the divergence for $k \to 0$. However, the integral from $k = 0$ to $k = k_m$ can be considered a constant C_0 determined also by the electronic configuration that does not govern the global behaviour for large angles to be derived here. Most importantly, the second moment in diffraction space is found to diverge logarithmically with the cut-off angle.

3.2.3. Numerical proof of logarithmic divergence

The neglect of low-angle details of the scattered intensity and multiple scattering as well as the assumption of plane wave incidence above lead to a compact analytical expression in eq. (9). It nevertheless needs to be validated by numerical simulations that account for these effects. To that end, we again turn towards the simulation employed in Fig. 12.

$\langle p^2 \rangle^{\mathrm{N}}_{\theta_l}$ was extracted while varying θ_l from 23 mrad to 499 mrad in steps of 4 mrad, and averaged over a scanning window covering one unit cell of the specimen for all available specimen thicknesses. The values taken by the

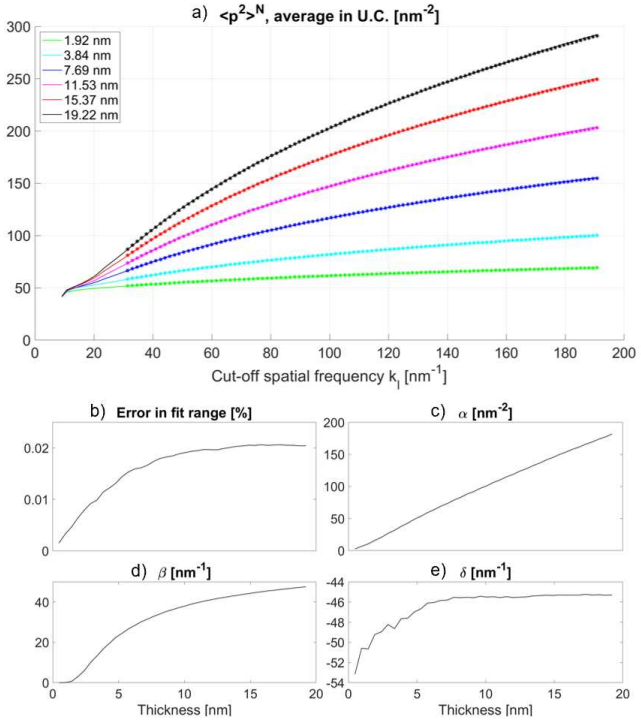

Figure 13: a) Results of the real-space average of $\langle p^2 \rangle^{\mathrm{N}}_{\theta_l}$ images, within one unit cell, for increasing cut-off frequencies k_l. The measurement is done with varying thickness, and a focus equal to zero. The curves are fitted with a parametric function, depicted as dot curves. b) Values taken by the fitting parameters α, β and δ, as well as the average quadratic error within the considered range, plotted as functions of thickness.

real-space average are plotted against θ_l in Fig. 13 a, for a selection of thicknesses. The curves were fitted [52] using a parametric function of the form

$$\langle p^2 \rangle^{\mathrm{N}}_{\theta_l} : \quad f(k_l) = \alpha \log\left(\frac{k_l - \delta}{\beta}\right) \quad , \tag{10}$$

while using α, β and δ as fit parameters. This parametric function was chosen consistently with eq. (9), with a spatial frequency offset δ included in the logarithm. This was done to allow the error minimization process to adapt the region of fitting by a lateral shift of the curve so as to represent the angular range where the actual logarithmic behaviour is present. In that regard, the fitted data points were restricted to a high-angle region covering $80 < \theta_l < 500$ mrad.

The fitted parametric function is plotted in Fig. 13 a as a dotted curve for each thickness referred to in the legend. Evidently, the logarithmic characteristics are indeed confirmed by the multislice results. The quadratic relative error of the fit is plotted in Fig. 13 b as a function of thickness. This error, averaged among the data points included within the $80 < \theta_l < 500$ mrad window, is observed to remain below 0.02 % in the thickness range considered. It however increases systematically with increasing thickness. This is likely related to the increment in the proportion of dynamically scattered electrons in the high-angle region, which are not included in the previous analytical approach, due to being limited to the Mott-Bethe relation. A plateau is reached at about 15 nm in thickness, which, in turn, could be due to the high-angle region being then dominated by TDS, here included through the frozen phonon approximation. The values taken by the parameters α, β and δ, respectively expressed in nm^{-2} and nm^{-1}, are also plotted against thickness in Fig. 13 c,d,e.

A remarkable linearity is found for the thickness dependence displayed by the parameter α. This, consistently with Fig. 12, shows that the domination of the high-angle contribution in $\langle p^2 \rangle^{\mathrm{N}}$ leads to dependencies to the specimen structure that can be exploited for the characterization of materials, and which are commonly found in the ADF imaging mode. The parameters β and δ, in the other hand, can be simply understood as offsets in the horizontal and vertical axes of Fig. 13 a. They thus act as additional degrees of freedom for the fitting process to be done on parts of the curve that better obey the logarithmic behavior. In that respect, the dependence shown by these two parameters reflect the quality of fit assessed in Fig. 13 b.

Note that the logarithmic divergence observed in Fig. 13 a is not affected by probe focus. This is because an incoherent average of the diffracted intensity over one unit cell leads to a cancellation of the aberration function [53].

Discussion

We found that different STEM techniques are affected by probe focus in a specific manner, depending on the geometry of the employed specimen. In particular, the focus

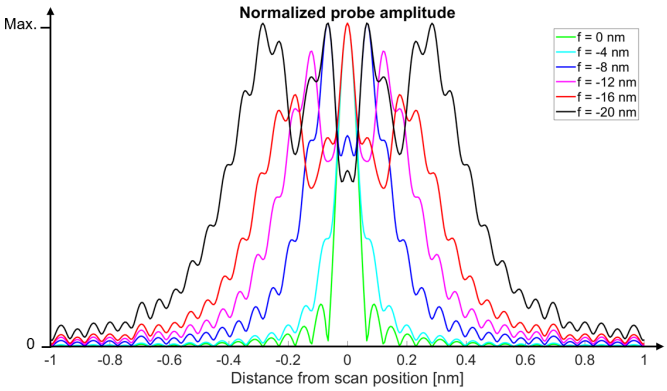

Figure 14: Profiles of the electron probe wave function (amplitude normalised to its maximum) in dependence of focus for 200 kV electrons and a semi-convergence angle of 23 mrad. Even for comparably large foci, the full width at half maximum is still within the range of 1 nm.

at which the contrast of the real-space image reaches a maximum is inherently signal-specific. This finding is especially relevant for the field of experimental condensed matter physics, because it translates into different specimen parameters being obtained with different sensitivities depending on the incident electron wave.

As a premise of this work, MR-STEM was shown to be employable to yield multiple information in parallel, such as thickness, chemical composition and electric field distribution. The different focus-dependence found among the STEM signals is therefore critical to this multidimensional approach, since the ideal conditions for all those measurements are potentially not all achievable through a single recording.

The most intuitive way to circumvent this limitation is the acquisition of a four-dimensional set of data for a series of probe foci. In that manner, a number of five measurement dimensions can be reached, though at the cost of experimental practicability. Due to currently available detector frame rates in the range of a few kHz, field of view, sampling and acquisition time are still constrained [1–8]. Nevertheless, hardware development progresses fast at present, such that FS-MR-STEM can be considered to become routinely feasible in practice in the coming years. This method has the supplementary advantage of yielding additional information, including the position of the interfaces between the specimen and vacuum in the vertical direction. This measurement was here shown to be best performed by employing the second moment in diffraction space, calculated as a function of scan position and probe focus, due to its robustness against limited variations of the angular cut-off.

The sensitivity to both top and bottom face of the specimen makes the method attractive to study local topography. However, when the probe is focused to the bottom surface, the top surface is scanned with an extended probe which puts a limit to the spatial resolution of the

method. Figure 14 shows simulated profiles for selected electron probes. The probe diameter is still below 1 nm in terms of the full width at half maximum even at a focus of −20 nm, which provides a figure of merit for the spatial resolution in mapping surface geometries.

As a new 4D STEM-specific signal, the second moment is especially relevant for scattering physics, not only because of its surface sensitivity, but also due to its high-angle characteristics, which can be understood in an analytical manner through a simple logarithmic model. In particular, a linear dependence to the thickness of the specimen was found for the parameter α in eq. (9), which is attractive for future work where thickness is a crucial parameter. In that respect, $\langle p^2 \rangle^{\mathrm{N}}$ has the additional advantage that it is, by the definition given in eq. (4), independent of the incident intensity and can be thus compared to simulation directly. In contrast, the quantitative HAADF imaging mode [42–44, 54, 55] provides thickness information by comparing experimental and scattered intensities normalised to the incident beam intensity, which needs to be measured in an additional experiment. Moreover, the present approach includes the precise knowledge of the diffraction coordinate system and thus of the cut-off angle, as well as the possibility to correct elliptical distortions in the recorded diffraction patterns.

To go further, simulating the propagation of electrons travelling at high angles to the optical axis in the projection system is challenging [56], such that the exploration of $\langle p^2 \rangle^{\mathrm{N}}$ up to relatively low angles in the range below 150 mrad could be attractive. On the other hand, a quantitative simulation of $\langle p^2 \rangle^{\mathrm{N}}$ needs to treat low-angle scattering accurately. In that respect, recent studies [9, 10, 57] point out a significant impact of inelastic scattering on the angular distribution of diffracted intensity due to, e.g., plasmon excitations. The impact of such processes on $\langle p^2 \rangle^{\mathrm{N}}$ is beyond the scope of this work and shall become a subject in future studies.

It is noteworthy that, to study the signal-specificity of the focus-dependencies, we additionally considered the influence of several supplementary factors in comprehensive simulations. This includes aberrations such as first-order and second-order astigmatism, spherical aberration and coma, partial coherence and carbon contamination. In the ranges expected for our experiment, we found that none of those factors would have significant impact on the conclusions drawn so far. The details of the influence of such experimental imperfections thus go beyond the scope of this work, but will be discussed in a further publication. Furthermore, the main features of the focus-dependence observed in the case study of In_2Se_3, including the surface effects and the fixation of the maximum electric fields sensitivity at a constant depth for thicknesses above a certain threshold, are in fact found in other materials. This was verified in supplementary multislice simulation work performed on bulk Au and $SrTiO_3$. This therefore shows the generality of our findings with regards to the exact specimen employed.

Summary and conclusion

In summary, we reported the sensitivity of MR-electron scattering to the focusing of a coherent probe in experiment and simulation. An automated acquisition scheme has been implemented in a scanning transmission electron microscope to yield atomically resolved focus-dependent 4D STEM data. It was found that conditions for maximum contrast differ among different signals such as Z-contrast images, coherent low-angle scattering as well as first and second moment imaging. In that respect, care must taken when considering a single momentum-resolved acquisition to provide universal STEM information. Most importantly, the second moment exhibits high sensitivity to the vertical location of specimen surfaces. Both the analytical and simulation-based analysis of the second moment characteristics with increasing cut-off angle revealed logarithmic divergence, which we used to derive a linear dependency on specimen thickness within parametric fits. To conclude, FS-MR-STEM provides fundamental insights into the scattering dynamics of relativistic electrons in crystals while providing detailed information about their shape, revealing dedicated contrast optima for signals that are sensitive to chemistry, thickness and electric fields.

Appendix A: Thickness measurement and assessment of specimen damage

Thickness estimation

For the purpose of measuring specimen thickness, a direct comparison of the simulated and experimental position-averaged convergent beam electron diffraction (PACBED) patterns was performed.

For an objective estimation, we determined the elliptical distortion parameters from the experimental pattern, depicted in Fig. 15 a, by fitting the rim of the undiffracted beam using the radial gradient method [1]. A distortion-corrected counterpart, with an interpolation done such that the resulting pixel size is 1 by 1 mrad is given in Fig. 15 b. This result was then compared to a simulation given in Fig. 15 d, itself interpolated from the raw simulation results depicted in Fig. 15 c in order to have the same sampling in simulation and experiment. The best agreement was found for a number of 7±1 vertically stacked unit cells, with a_c=1.92 nm. A specimen mistilt of 1.7±0.5 mrad was additionally determined.

Specimen damage and contamination

The quadratic averaged intensity of the experimental PACBED pattern, as measured within the primary beam, does not vary more than 1 %, thus demonstrating the absence of specimen damage throughout the acquisition. Given this, carbon contamination can additionally be estimated to be negligible, as the average HAADF intensity detected through the series does not vary in a systematic manner, with possible variations remaining below 1 % as well.

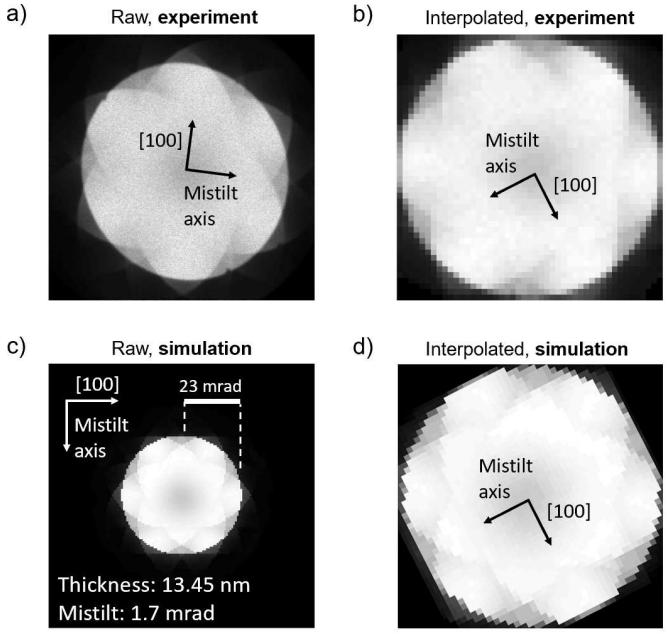

Figure 15: Comparison of position-averaged diffraction features between experiment and simulation. a) Experimental and c) simulated PACBED patterns are given both directly and b,d) after a distortion correction step, followed by an interpolation done such that each pixel displayed is 1 by 1 mrad in size.

Appendix B: calculation of divergence and integral using finite differences in a five-point stencil

In this work, the divergence ρ and integral ϕ of $\langle\vec{p}\rangle^{\mathrm{N}}$ are obtained through a five-point-stencil calculation scheme. Below, we give the details of its derivation through finite differences.

We begin by writing explicitly

$$\langle\vec{p}\rangle^{\mathrm{N}}(x,y) = [\,p_x(x,y)\,;\,p_y(x,y)\,]$$

such that

$$\rho(x,y) = \frac{\partial p_x(x,y)}{\partial x} + \frac{\partial p_y(x,y)}{\partial y}$$

and

$$[\,p_x(x,y)\,;\,p_y(x,y)\,] = \left[\,\frac{\partial\phi(x,y)}{\partial x}\,;\,\frac{\partial\phi(x,y)}{\partial y}\,\right] \quad .$$

Using finite differences, we can approximate the derivation of $[\,p_x(x,y)\,;\,p_y(x,y)\,]$ by $[\,x\,;\,y\,]$ through

$$\frac{\partial p_x(x,y)}{\partial x} = \frac{p_x(x+\delta x,y) - p_x(x-\delta x,y)}{2\delta x}$$

$$\frac{\partial p_y(x,y)}{\partial y} = \frac{p_y(x,y+\delta y) - p_y(x,y-\delta y)}{2\delta y} \quad .$$

In that manner, and while identifying $\delta r = \delta x = \delta y$ to the pixel size of the scan window, the extraction of ρ can be done both easily by means of calculating

$$\rho = \frac{D_x(x,y) + D_y(x,y)}{2\delta r}$$

with

$$D_x(x,y) = p_x(x+\delta x,y) - p_x(x-\delta x,y)$$

$$D_y(x,y) = p_y(x,y+\delta y) - p_y(x,y-\delta y) \quad .$$

The calculation of ϕ is done afterward using the relation between $\phi(x,y)$ and $\rho(x,y)$

$$\rho(x,y) = \Delta\phi(x,y) = \frac{\partial^2\phi(x,y)}{\partial x^2} + \frac{\partial^2\phi(x,y)}{\partial y^2} \quad ,$$

with the second-order derivatives being given by

$$\frac{\partial^2\phi(x,y)}{\partial x^2} = \frac{\phi(x+\delta x,y) - 2\phi(x,y) + \phi(x-\delta x,y)}{\delta x^2}$$

$$\frac{\partial^2\phi(x,y)}{\partial y^2} = \frac{\phi(x,y+\delta y) - 2\phi(x,y) + \phi(x,y-\delta y)}{\delta y^2} \quad .$$

By assigning $\delta r = \delta x = \delta y$ again, this results in

$$\rho(x,y) = \frac{F(x,y) - 4\phi(x,y)}{\delta r^2}$$

with

$$F(x,y) = \phi(x+\delta r,y)+\phi(x-\delta r,y)+\phi(x,y+\delta r)+\phi(x,y-\delta r) \quad .$$

$\phi(x,y)$ can then be obtained from $\rho(x,y)$ by iterating

$$\phi^{n+1}(x,y) = \frac{F_r^n(x,y) - \delta r^2\rho(x,y)}{4} \quad ,$$

a sufficient number of times.

Using this technique, the extraction of the integral ϕ from the first moment map $\langle\vec{p}\rangle^{\mathrm{N}}$ can be reliably performed with low sensitivity to noise, due to the successive subtraction and summation of neighboring pixels in the vector map, and no reconstruction artefacts. Nevertheless, the process itself, in particular with the requirement of a user-defined number of iterations, may be slightly time-consuming in comparison to other methods such as the Fourier integration [47]. This is however not a notable limitation, unless the calculation has to be done live.

Acknowledgements

We thank Dr. Florian Winkler for valuable discussions and experimental work at the early stages of this study. This work was supported by the Initiative and Network Fund of the Helmholtz Association (Germany) under contracts VH-NG-1317 and ZT-I-0025. This project furthermore received funding from the European Research Council (ERC) under the European Union's Horizon 2020 research and innovation program (grant agreement No. 770887).

Declaration of conflicts of interest

The authors declare no conflicts of interest.

References

[1] K. Müller, H. Ryll, I. Ordavo, S. Ihle, L. Strüder, K. Volz, J. Zweck, H. Soltau, A. Rosenauer, Scanning transmission electron microscopy strain measurement from millisecond frames of a direct electron charge coupled device, Appl. Phys. Lett. 101 (21) (2012) 212110. doi:10.1063/1.4767655.

[2] H. Ryll, M. Simson, R. Hartmann, P. Holl, M. Huth, S. Ihle, Y. Kondo, P. Kotula, A. Liebel, K. Müller-Caspary, A. Rosenauer, R. Sagawa, J. Schmidt, H. Soltau, L. Strüder, A pnCCD-based, fast direct single electron imaging camera for TEM and STEM, J. Instrum. 11 (04) (2016) P04006. doi:10.1088/1748-0221/11/04/P04006.

[3] G. McMullan, D. M. Cattermole, S. Chen, R. Henderson, X. Llopart, C. Summerfield, L. Tlustos, A. R. Faruqi, Electron imaging with Medipix2 hybrid pixel detector, Ultramicroscopy 107 (4-5) (2007) 401–413. doi:10.1016/j.ultramic.2006.10.005.

[4] K. Müller-Caspary, A. Oelsner, P. Potapov, Two-dimensional strain mapping in semiconductors by nano-beam electron diffraction employing a delay-line detector, Appl. Phys. Lett. 107 (7) (2015) 72110. doi:10.1063/1.4927837.

[5] R. Plackett, I. Horswell, E. N. Gimenez, J. Marchal, D. Omar, N. Tartoni, Merlin: a fast versatile readout system for Medipix3, Journal of Instrumentation 8 (1) (2013) C01038. doi:10.1088/1748-0221/8/01/C01038.

[6] M. W. Tate, P. Purohit, D. Chamberlain, K. X. Nguyen, R. Hovden, C. S. Chang, P. Deb, E. Turgut, J. T. Heron, D. G. Schlom, D. C. Ralph, G. D. Fuchs, K. S. Shanks, H. T. Philipp, D. A. Muller, S. M. Gruner, High Dynamic Range Pixel Array Detector for Scanning Transmission Electron Microscopy, Microsc. Microanal. 22 (1) (2016) 237–249. arXiv:1511.03539, doi:10.1017/S1431927615015664.

[7] R. Ballabriga, M. Campbell, E. Heijne, X. Llopart, L. Tlustos, W. Wong, Medipix3: A 64 k pixel detector readout chip working in single photon counting mode with improved spectrometric performance, in: Nuclear Instruments and Methods in Physics Research, Section A: Accelerators, Spectrometers, Detectors and Associated Equipment, Vol. 633, 2011. doi:10.1016/j.nima.2010.06.108.

[8] G. McMullan, A. R. Faruqi, R. Henderson, Direct Electron Detectors, in: Methods in Enzymology, Vol. 579, Academic Press Inc., 2016, pp. 1–17. doi:10.1016/bs.mie.2016.05.056.

[9] A. Beyer, F. F. Krause, H. L. Robert, S. Firoozabadi, T. Grieb, P. Kükelhan, D. Heimes, M. Schowalter, K. Müller-Caspary, A. Rosenauer, K. Volz, Influence of plasmon excitations on atomic-resolution quantitative 4D scanning transmission electron microscopy, Scientific Reports 10 (1) (2020) 1–15. doi:10.1038/s41598-020-74434-w.

[10] K. Müller-Caspary, O. Oppermann, T. Grieb, F. F. Krause, A. Rosenauer, M. Schowalter, T. Mehrtens, A. Beyer, K. Volz, P. Potapov, Materials characterisation by angle-resolved scanning transmission electron microscopy, Scientific Reports 6 (April) (2016) 1–9. doi:10.1038/srep37146.

[11] J. M. Rodenburg, R. H. T. Bates, The Theory of Super-Resolution Electron Microscopy Via Wigner-Distribution Deconvolution, Philosophical Transactions Section A: Physical Sciences and Engineering 339 (1655) (1992) 521–553. doi:10.1098/rsta.1992.0050.

[12] J. M. Rodenburg, B. C. Mccallum, P. D. Nellist, J. M. Rodenburg, B. C. McCallum, P. D. Nell isn't, J. M. Rodenburg, B. C. Mccallum, P. D. Nellist, J. M. Rodenburg, B. C. McCallum, P. D. Nell isn't, Experimental tests on double-resolution coherent imaging via STEM, Ultramicroscopy 48 (1993) 304–314. doi:10.1016/0304-3991(93)90105-7.

[13] T. J. Pennycook, A. R. Lupini, H. Yang, M. F. Murfitt, L. Jones, P. D. Nellist, Efficient phase contrast imaging in {STEM} using a pixelated detector. Part 1: Experimental demonstration at atomic resolution, Ultramicroscopy 151 (0) (2015) 160–167. doi:http://dx.doi.org/10.1016/j.ultramic.2014.09.013.

[14] H. Yang, R. N. Rutte, L. Jones, M. Simson, R. Sagawa, H. Ryll, M. Huth, T. J. Pennycook, M. L. H. Green, H. Soltau, Y. Kondo, B. G. Davis, P. D. Nellist, Simultaneous atomic-resolution electron ptychography and Z-contrast imaging of light and heavy elements in complex nanostructures, Nature Comm. 7 (2016) 12532. doi:10.1038/ncomms12532.

[15] J. Rodenburg, A. Maiden, Ptychography, in: Springer Handbooks, Springer, 2019, pp. 819–904. doi:10.1007/978-3-030-00069-1_17.

[16] H. Yang, T. J. Pennycook, P. D. Nellist, Efficient phase contrast imaging in STEM using a pixelated detector. Part II: Optimisation of imaging conditions, Ultramicroscopy 151 (0) (2015) 232–239. doi:10.1016/j.ultramic.2014.10.013.

[17] H. Yang, L. Jones, H. Ryll, M. Simson, H. Soltau, Y. Kondo, R. Sagawa, H. Banba, I. MacLaren, P. D. Nellist, 4D STEM: High efficiency phase contrast imaging using a fast pixelated detector, J. Phys.: Conf. Ser. 644 (1) (2015) 12032. doi:10.1088/1742-6596/644/1/012032.

[18] Y. Jiang, Z. Chen, Y. Han, P. Deb, H. Gao, S. Xie, P. Purohit, M. W. Tate, J. Park, S. M. Gruner, V. Elser, D. A. Muller, Electron ptychography of 2D materials to deep sub-ångström resolution, Nature 559 (7714) (2018) 343–349. doi:10.1038/s41586-018-0298-5.

[19] K. Müller, F. F. Krause, A. Beche, M. Schowalter, V. Galioit, S. Löffler, J. Verbeeck, J. Zweck, P. Schattschneider, A. Rosenauer, A. Béché, M. Schowalter, V. Galioit, S. Löffler, J. Verbeeck, J. Zweck, P. Schattschneider, A. Rosenauer, Atomic electric fields revealed by a quantum mechanical approach to electron picodiffraction, Nature Communications 5 (2014) 5653:1–8. doi:10.1038/ncomms6653.

[20] K. Müller-Caspary, M. Duchamp, M. Rösner, V. Migunov, F. Winkler, H. Yang, M. Huth, R. Ritz, M. Simson, S. Ihle, H. Soltau, T. Wehling, R. E. Dunin-Borkowski, S. Van Aert, A. Rosenauer, Atomic-scale quantification of charge densities in two-dimensional materials, Physical Review B 98 (12) (sep 2018). doi:10.1103/PhysRevB.98.121408.

[21] K. Müller-Caspary, T. Grieb, J. Müßener, N. Gauquelin, P. Hille, J. Schörmann, J. Verbeeck, S. Van Aert, M. Eickhoff, A. Rosenauer, Electrical Polarization in AlN/GaN Nanodisks Measured by Momentum-Resolved 4D Scanning Transmission Electron Microscopy, Physical Review Letters 122 (10) (2019) 106102. doi:10.1103/PhysRevLett.122.106102.

[22] D. A. Muller, K. X. Nguyen, M. W. Tate, P. Purohit, C. Chang, M. Cao, S. M. Gruner, An Electron Microscope Pixel Array Detector as a Universal STEM Detector, Microscopy and Microanalysis 22 (S3) (2016) 478–479. doi:10.1017/s143192761600324x.

[23] J. A. Hachtel, J. C. Idrobo, M. Chi, Sub-Ångstrom electric field measurements on a universal detector in a scanning transmission electron microscope, Advanced Structural and Chemical Imaging 4 (1) (2018). doi:10.1186/s40679-018-0059-4.

[24] K. van Benthem, A. R. Lupini, M. P. Oxley, S. D. Findlay, L. J. Allen, S. J. Pennycook, Three-dimensional ADF imaging of individual atoms by through-focal series scanning transmission electron microscopy, Ultramicroscopy 106 (11-12 SPEC. ISS.) (2006) 1062–1068. doi:10.1016/j.ultramic.2006.04.020.

[25] H. L. Xin, V. Intaraprasonk, D. A. Muller, Depth sectioning of individual dopant atoms with aberration-corrected scanning transmission electron microscopy, Applied Physics Letters 92 (1) (2008) 1–4. doi:10.1063/1.2828990.

[26] H. Yang, J. G. Lozano, T. J. Pennycook, L. Jones, P. B. Hirsch, P. D. Nellist, Imaging screw dislocations at atomic resolution by aberration-corrected electron optical sectioning, Nature Communications 6 (June) (2015) 1–7. doi:10.1038/ncomms8266.

[27] R. Ishikawa, S. J. Pennycook, A. R. Lupini, S. D. Findlay, N. Shibata, Y. Ikuhara, Single atom visibility in STEM opti-

cal depth sectioning, Applied Physics Letters 109 (16) (2016). doi:10.1063/1.4965709.

[28] M. Alania, T. Altantzis, A. De Backer, I. Lobato, S. Bals, S. Van Aert, Depth sectioning combined with atom-counting in HAADF STEM to retrieve the 3D atomic structure, Ultramicroscopy 177 (2017) 36–42. doi:10.1016/j.ultramic.2016.11.002.

[29] S. D. Findlay, N. Shibata, H. Sawada, E. Okunishi, Y. Kondo, Y. Ikuhara, Dynamics of annular bright field imaging in scanning transmission electron microscopy, Ultramicroscopy 110 (7) (2010) 903–923. doi:http://dx.doi.org/10.1016/j.ultramic.2010.04.004.

[30] P. Gao, A. Kumamoto, R. Ishikawa, N. Lugg, N. Shibata, Y. Ikuhara, Picometer-scale atom position analysis in annular bright-field STEM imaging, Ultramicroscopy 184 (2018) 177–187. doi:10.1016/j.ultramic.2017.09.001.

[31] C. Addiego, W. Gao, X. Pan, Thickness and defocus dependence of inter-atomic electric fields measured by scanning diffraction, Ultramicroscopy 208 (September 2019) (2020) 112850. doi:10.1016/j.ultramic.2019.112850.

[32] J. Bürger, T. Riedl, J. K. Lindner, Influence of lens aberrations, specimen thickness and tilt on differential phase contrast STEM images, Ultramicroscopy 219 (February) (2020) 113118. doi:10.1016/j.ultramic.2020.113118.

[33] K. Momma, F. Izumi, VESTA 3 for three-dimensional visualization of crystal, volumetric and morphology data, Journal of Applied Crystallography 44 (6) (2011) 1272–1276. doi:10.1107/S0021889811038970.

[34] M. Küpers, P. M. Konze, A. Meledin, J. Mayer, U. Englert, M. Wuttig, R. Dronskowski, Controlled Crystal Growth of Indium Selenide, In2Se3, and the Crystal Structures of α-In2Se3, Inorganic Chemistry 57 (18) (2018) 11775–11781. doi:10.1021/acs.inorgchem.8b01950.

[35] D. Box, G. Booch, C. Kindel, Essential COM, 1st Edition, Addison-Wesley Longman Publishing Co., Inc., USA, 1997.

[36] J. M. Cowley, A. F. Moodie, The scattering of electrons by atoms and crystals. I. A new theoretical approach, Acta Crystallogr. 10 (10) (1957) 609–619. doi:10.1107/S0365110X57002194.

[37] D. Van Dyck, Is the frozen phonon model adequate to describe inelastic phonon scattering?, Ultramicroscopy 109 (6) (2009) 677–682. doi:10.1016/j.ultramic.2009.01.001.

[38] F. F. Krause, A. Rosenauer, Reciprocity relations in transmission electron microscopy: A rigorous derivation, Micron 92 (Supplement C) (2017) 1–5. doi:10.1016/j.micron.2016.09.007.

[39] D. Zhou, K. Müller-Caspary, W. Sigle, F. F. Krause, A. Rosenauer, P. A. van Aken, Sample tilt effects on atom column position determination in ABF-STEM imaging, Ultramicroscopy 160 (2016) 110–117. doi:10.1016/j.ultramic.2015.10.008.

[40] Y. M. Kim, S. J. Pennycook, A. Y. Borisevich, Quantitative comparison of bright field and annular bright field imaging modes for characterization of oxygen octahedral tilts, Ultramicroscopy 181 (2017) 1–7. doi:10.1016/j.ultramic.2017.04.020.

[41] K. Müller-Caspary, F. F. Krause, T. Grieb, S. Löffler, M. Schowalter, A. Béché, V. Galioit, D. Marquardt, J. Zweck, P. Schattschneider, J. Verbeeck, A. Rosenauer, Measurement of atomic electric fields and charge densities from average momentum transfers using scanning transmission electron microscopy, Ultramicroscopy 178 (2017) 62–80. doi:10.1016/j.ultramic.2016.05.004.

[42] J. M. LeBeau, S. Stemmer, Experimental quantification of annular dark-field images in scanning transmission electron microscopy, Ultramicroscopy 108 (2008) 1653–1658. doi:10.1016/j.ultramic.2008.07.001.

[43] J. M. Lebeau, S. D. Findlay, X. Wang, A. J. Jacobson, L. J. Allen, S. Stemmer, High-angle scattering of fast electrons from crystals containing heavy elements: Simulation and experiment, Physical Review B - Condensed Matter and Materials Physics 79 (21) (jun 2009). doi:10.1103/PhysRevB.79.214110.

[44] A. Rosenauer, K. Gries, K. Müller, A. Pretorius, M. Schowalter, A. Avramescu, K. Engl, S. Lutgen, Measurement of specimen thickness and composition in Alx Ga1 - x N / GaN using high-angle annular dark field images, Ultramicroscopy 109 (9) (2009) 1171–1182. doi:10.1016/j.ultramic.2009.05.003.

[45] T. Grieb, K. Müller, E. Cadel, A. Beyer, M. Schowalter, E. Talbot, K. Volz, A. Rosenauer, Simultaneous Quantification of Indium and Nitrogen Concentration in InGaNAs Using HAADF-STEM, Microsc. Microanal. 20 (06) (2014) 1740–1752. doi:10.1017/S1431927614013051.

[46] G. Ruben, E. C. Cosgriff, A. J. D'Alfonso, S. D. Findlay, J. M. LeBeau, L. J. Allen, Interface location by depth sectioning using a low-angle annular dark field detector, Ultramicroscopy 113 (2012) 131–138. doi:10.1016/j.ultramic.2011.11.002.

[47] I. Lazić, E. G. T. Bosch, S. Lazar, Phase contrast {STEM} for thin samples: Integrated differential phase contrast, Ultramicroscopy 160 (2016) 265–280. doi:http://doi.org/10.1016/j.ultramic.2015.10.011.

[48] A. Beyer, R. Straubinger, J. Belz, K. Volz, Local sample thickness determination via scanning transmission electron microscopy defocus series, Journal of Microscopy 262 (2) (2016) 171–177. doi:10.1111/jmi.12284.

[49] H. Bethe, Theorie der Beugung von Elektronen an Kristallen, Ann. Phys. 87 (1928) 55–129.

[50] N. F. Mott, The Scattering of Electrons by Atoms, Proc. Roy. Soc. Lond. A 127 (806) (1930) 658–665. doi:10.1098/rspa.1930.0082.

[51] P. Geuens, D. Van Dyck, The S-state model for electron channeling in high-resolution electron microscopy, Advances in Imaging and Electron Physics 136 (2005) 111–226. doi:10.1016/S1076-5670(04)36002-7.

[52] J. C. Lagarias, J. A. Reeds, M. H. Wright, P. E. Wright, Convergence properties of the Nelder-Mead simplex method in low dimensions, SIAM Journal on Optimization 9 (1) (1998) 112–147. doi:10.1137/S1052623496303470.

[53] J. M. LeBeau, S. D. Findlay, L. J. Allen, S. Stemmer, Position averaged convergent beam electron diffraction: Theory and applications, Ultramicroscopy 110 (2) (2010) 118–125. doi:10.1016/j.ultramic.2009.10.001.

[54] A. Rosenauer, T. Mehrtens, K. Müller, K. Gries, M. Schowalter, P. V. Satyam, S. Bley, C. Tessarek, D. Hommel, K. Sebald, M. Seyfried, J. Gutowski, A. Avramescu, K. Engl, S. Lutgen, Composition mapping in InGaN by scanning transmission electron microscopy, Ultramicroscopy 111 (2011) 1316–1327. doi:DOI:10.1016/j.ultramic.2011.04.009.

[55] J. M. LeBeau, S. D. Findlay, L. J. Allen, S. Stemmer, Quantitative Atomic Resolution Scanning Transmission Electron Microscopy, Phys. Rev. Lett. 100 (20) (2008) 206101. doi:10.1103/PhysRevLett.100.206101.

[56] F. F. Krause, M. Schowalter, T. Grieb, K. Müller-Caspary, T. Mehrtens, A. Rosenauer, Effects of instrument imperfections on quantitative scanning transmission electron microscopy, Ultramicroscopy 161 (2016) 146–160. doi:http://dx.doi.org/10.1016/j.ultramic.2015.10.026.

[57] T. Grieb, F. F. Krause, K. Müller-Caspary, S. Firoozabadi, C. Mahr, M. Schowalter, A. Beyer, O. Oppermann, K. Volz, A. Rosenauer, Angle-resolved STEM using an iris aperture: Scattering contributions and sources of error for the quantitative analysis in Si, Ultramicroscopy 221 (October 2020) (2021) 113175. doi:10.1016/j.ultramic.2020.113175.